J. Kongthon
e-mail: jiradech@u.washington.edu

J.-H. Chung
e-mail: jae71@u.washington.edu

J. J. Riley
e-mail: rileyj@u.washington.edu

S. Devasia[1]
e-mail: devasia@u.washington.edu

Mechanical Engineering Department,
University of Washington,
Seattle WA 98195-2600

Dynamics of Cilia-Based Microfluidic Devices

This article models the dynamics of cilia-based devices (soft cantilever-type, vibrating devices that are excited by external vibrations) for mixing and manipulating liquids in microfluidic applications. The main contribution of this article is to develop a model, which shows that liquid sloshing and the added-mass effect play substantial roles in generating large-amplitude motion of the cilia. Additionally, experimental mixing results, with and without cilia, are comparatively evaluated to show more than one order-of-magnitude reduction in the mixing time with the use of cilia. [DOI: 10.1115/1.4004063]

1 Introduction

This article models the dynamics of cilia-based devices (soft cantilever-type vibrating devices that are excited by external vibrations) for mixing and manipulating liquids in microfluidic applications. The behavior of biological cilia, discovered by Anton de Heide in 1684 [1], has been studied in, e.g., Refs. [1–6]. Biomimetic, cilia-like structures have been proposed for a variety of applications such as nasal filters [7] and sample transport [8]. In microfluidics, biomimetic actuators have been proposed for mixing and manipulation in liquid environments [9–15]. The main contribution of this article is to develop a model for a cilia-based device, which shows that the liquid sloshing (e.g., Refs. [16,17]) and the added-mass effect (e.g., Refs. [18–21]) play substantial roles in generating large-amplitude motion of the cilia in liquid when the chamber containing the cilia is oscillated to mechanically excite the cilia resonance. Additionally, experimental results are presented to show that the average mixing time with cilia is more than one order-of-magnitude lower than the average mixing time without cilia.

Mixing can be improved by generating complex flows in the fluid to overcome the mixing-rate limits of laminar flows that are typical at the microscale. For example, passive techniques such as channels with patterned grooves can be used to generate chaotic folding (and refolding) of the liquid as it flows past the grooves to improve mixing [22]. Such flow-type mixing can be used when a sufficiently large amount of sample is available to achieve the flow through the grooved channel. In contrast, if the amount of sample is limited, then batch-type mixing is sought in small chambers containing the sample. Batch mixing can be enhanced using a variety of actuation techniques such as high-frequency ultrasound excitation [23,24] and time-varying external magnetic fields [14,25–27]. In the current work, cilia are excited by low-frequency oscillations (compared to higher-frequency acoustic excitation) of the chamber containing the sample. This low-frequency mechanical excitation of cilia is advantageous for mixing samples that are susceptible to damage from high-frequency excitation and magnetic fields. The current article shows that batch mixing can be substantially improved by using cilia when compared to the case without cilia—for the same oscillatory actuation of the chamber.

The main contribution of the article is to develop a model that explains the large-amplitude cilia motion in the liquid. In general, it is difficult to generate large amplitude motion of cilia-type devices in the presence of substantial fluid damping [28,29]. For example, the damping ratio ζ in liquid tends to be in the range of 0.05–0.5 [28], which leads to a small (1.7–1.9) amplification factor (i.e., ratio of the cilia-tip motion to the excitation of the chamber) at the vibrational resonance of cilia. The current work shows that sloshing in the chambers containing the cilia can be exploited to achieve large (3–4) amplification factors. Previous work has shown that the sloshing phenomena, which is well studied in literature for large-scale systems (e.g., Refs. [16,17]), is also important in microsystems [30]. In the current article, such sloshing models are used to explain the large-amplitude motion of cilia observed in the experiments.

The proposed model is used to show that the added-mass effect in fluid-structure interactions should be considered to capture the excitation of the cilia resonance by the sloshing. It is noted that the added-mass effect is important in other applications, such as underwater vehicles [31] and atomic force microscopy [28], and was introduced in early works on pendulum oscillations initiated by Dubuat—an early history of the added mass by Stokes can be found in Ref. [18]. In cilia-based devices, the added mass has been shown to reduce the resonance frequency of the cilia in liquid when compared to cilia in air [32]. The current article shows that the lowering of the cilia's vibrational frequency to be close to the sloshing resonance frequency of the chamber results in an increased excitation of the cilia resonance by the sloshing. Thereby, the added-mass effect plays a significant role in achieving large-amplitude, cilia motion.

2 Modeling the Cilia Dynamics

2.1 System Description. The displacement along the length (x) of a cilium is excited by the motion ($u_b(t)$) of the cilia base by using a piezoactuator (Burleigh PZS200) as shown in Fig. 1. The soft cilia are fabricated from polydimethylsiloxane (PDMS) using a silicon mold. Detailed information on cilia fabrication and material properties can be found in Ref. [13]. The nominal dimensions of the silicon mold used to fabricate the cilia used in the experiments are length ($L = 800$ μm), height ($H = 45$ μm), and depth ($D = 10$ μm). An oscillatory motion

$$u_c(t) = A\sin(\omega t)$$

of the chamber containing the cilia is achieved by using a piezoactuator as shown in Fig. 1 where A and ω are the amplitude and the frequency of the oscillation, respectively. The input $u_b(t)$ of the system is the motion of the base of the cilia, which is the same as the oscillatory motion of the chamber because the cilia base is attached to the chamber with a relatively stiff structure, i.e.,

$$u_b(t) = u_c(t)$$

[1]Corresponding author.

Contributed by the Dynamic Systems Division of ASME for publication in the JOURNAL OF DYNAMIC SYSTEMS, MEASUREMENT, AND CONTROL. Manuscript received September 1, 2010; final manuscript received March 1, 2011; published online August 22, 2011. Assoc. Editor: Nariman Sepehri.

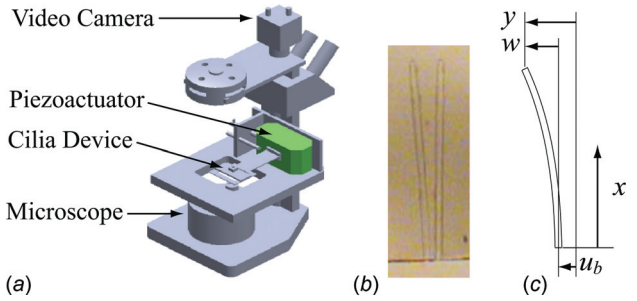

Fig. 1 Schematics of experiment for evaluating the frequency response of cilia. (*a*) Experimental setup; (*b*) image of a cilium in water excited by the piezoactuator; (*c*) input $u_b(t)$ and output $y(t)$ motions of the cilium.

The output of the system is the motion

$$y(t) = \hat{y}(L,t)$$

of the cilia tip, i.e., at the free end with $x = L$, as shown in Fig. 1(*c*).

The input (cilia-base motion $u_b(t)$) and the output (cilia-tip motion $y(t)$) are observed by using an optical microscope with a charge coupled device (CCD) camera and the displacement amplitude of the vibrating cilia is measured using captured still images (Pinnacle Studio Version 12). A typical image of the resulting cilia vibration (due to the chamber oscillation) is shown in Fig. 1(*b*).

2.2 Euler–Bernoulli Model of Cilia Vibration. The Euler–Bernoulli beam approach, e.g., Ref. [33], is used to model the vibrational response of the cantilever-type cilia device—such standard beam theory has been used in the past to model the dynamics of microscale cantilevers in the liquid [28,29,32]. In particular, the dynamics of the net motion $\hat{y}(x,t)$ of a vibrating cilium (beam) is given by

$$\rho_b A_b \frac{\partial^2 \hat{y}(x,t)}{\partial t^2} + EI \frac{\partial^4 \hat{y}(x,t)}{\partial x^4} = f(x,t) \tag{1}$$

where the subscript b represents a property of the beam, ρ_b is the mass density, $A_b = DH$ is the cross sectional area, E is the Young's modulus, and $I = HD^3/12$ is the area moment of inertia. The net motion $\hat{y}(x,t)$ is composed of the base motion, i.e., the input $u_b(t)$, and the elastic deflection, $\hat{w}(x,t)$ of the cilium (beam)

$$\hat{y}(x,t) = \hat{w}(x,t) + u_b(t) \tag{2}$$

as illustrated in Fig. 1(*c*), and standard cantilever boundary conditions

$$\hat{w}(0,t) = 0, \quad \frac{\partial \hat{w}(0,t)}{\partial x} = 0, \quad \frac{\partial^2 \hat{w}(L,t)}{\partial x^2} = 0, \quad \frac{\partial^3 \hat{w}(L,t)}{\partial x^3} = 0 \tag{3}$$

The first term on the left hand side of Eq. (1) represents the inertial effects, the second term on the left hand side of Eq. (1) represents the elastic effects, and $f(x,t)$ (on the right hand side) represents the total external force (per unit length) on the cilium. The external forces acting on the cilium are described next.

2.2.1 External Forces. The external force f acting on the cilium (in Eq. (1)) has four parts: (i) the drag (friction) force f_f between the cilium and the fluid; (ii) the internal damping force f_i; (iii) the inertial load f_m due to the added-mass effect; and (iv) the buoyancylike force f_b due to the fluid acceleration

$$f(x,t) = f_f(x,t) + f_i(x,t) + f_m(x,t) + f_b(x,t) \tag{4}$$

2.2.1.1 Drag force. The first term in Eq. (4), the distributed drag force f_f due to hydrodynamic interaction, depends on the relative velocity between the structure and the fluid; it is approximated as (similar to [34,35])

$$f_f(x,t) = -B_f \left[\frac{\partial \hat{y}(x,t)}{\partial t} - \dot{u}_f \right] = -B_f \left[\frac{\partial \hat{w}(x,t)}{\partial t} + \dot{u}_b - \dot{u}_f \right] \tag{5}$$

where B_f is the fluid damping parameter that depends on the flow conditions and $\dot{u}_f$ is the fluid velocity.

2.2.1.2 Internal damping. The second term in Eq. (4), the internal damping force f_i, depends on the rate of change of the beam's elastic deflection and is described by

$$f_i(x,t) = -B_i \left[\frac{\partial \hat{w}(x,t)}{\partial t} \right] \tag{6}$$

where B_i is the internal damping parameter that depends on the beam properties.

2.2.1.3 Inertial loading. The third term in Eq. (4), the inertial load f_m, arises because of the need to accelerate the fluid surrounding an object when the object is accelerated through a fluid [18–21]. The inertia of the fluid exerts a resistive force on the object; this resistive force is termed as the *added-mass effect* because the object responds as if its mass has increased. This added-mass effect can be modeled as an inertial forcing term (f_m) that depends on the relative acceleration between the beam and the fluid as

$$\begin{aligned} f_m(x,t) &= -\rho_f A_f \left[\frac{\partial^2 \hat{y}(x,t)}{\partial t^2} - \ddot{u}_f(t) \right] \\ &= -\rho_f A_f \left[\frac{\partial^2 \hat{w}(x,t)}{\partial t^2} + \ddot{u}_b(t) - \ddot{u}_f(t) \right] \end{aligned} \tag{7}$$

where A_f is the effective hydrodynamic area of the fluid that affects the inertial force f_m (per unit length) and ρ_f is the fluid density. The hydrodynamic mass $\rho_f A_f$ of the fluid (per unit length) that affects the inertial loading can be described in terms of the corresponding beam mass $\rho_b A_b$ (per unit length) and an added-mass coefficient C_m as [32]

$$\rho_f A_f = C_m \rho_b A_b \tag{8}$$

Thus, the inertial load f_m (in Eq. (7)) can be rewritten in terms of the added-mass coefficient C_m by using Eq. (8) as

$$f_m(x,t) = -C_m \rho_b A_b \left[\frac{\partial^2 \hat{w}(x,t)}{\partial t^2} + \ddot{u}_b(t) - \ddot{u}_f(t) \right] \tag{9}$$

2.2.1.4 Buoyancy-like force. The last term in Eq. (4), f_b, called the buoyancy force in [36] (Chap. 6, page 120) is also referred to as the Froude–Krylov force in Ref. [37] (Chap. 4, page 131). This force arises due to the pressure gradient P' across the depth D of the cilium due to the fluid acceleration $\ddot{u}_f(t)$, which is given by

$$P' = -\rho_f \ddot{u}_f(t) \tag{10}$$

This pressure gradient results in a difference in forces acting on the cilium due to the variations in the pressure P as shown in Fig. 2 for a small length L_b of the cilium—this is similar to the net buoyancy force due to the standard gravity-related pressure gradient. The resulting force (per unit length) acting on the cilium is given by

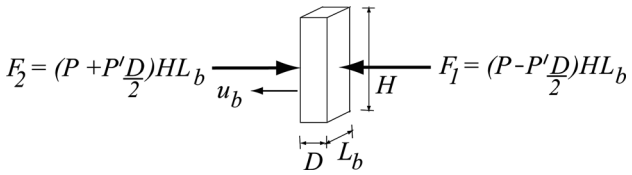

Fig. 2 Pressure gradient due to accelerating fluid generates buoyancylike force across the thickness of a cilium

$$f_b(x,t) = \frac{F_1 - F_2}{L_b} = \frac{(P - P'D/2)HL_b - (P + P'D/2)HL_b}{L_b} = -P'DH \quad = -P'A_b = \rho_f A_b \ddot{u}_f(t) \tag{11}$$

Substituting the different terms in the external force f (Eq. (4)) into the the Euler–Bernoulli equation for the cilium dynamics (Eq. (1))—i.e., the drag (friction) force f_f from Eq. (5), the internal damping force f_i from Eq. (6), the inertial load f_m from Eq. (9), and the buoyancy-like force f_b from Eq. (11)—and then collecting similar terms in the cilium deflection w, input u_b, and fluid motion u_f leads to

$$\frac{\partial^2 \hat{w}(x,t)}{\partial t^2} + \frac{(B_f + B_i)}{\rho_b A_b (1 + C_m)} \frac{\partial \hat{w}(x,t)}{\partial t} + \frac{EI}{\rho_b A_b (1 + C_m)} \frac{\partial^4 \hat{w}(x,t)}{\partial x^4} = r(t) \tag{12}$$

with the forcing term $r(t)$ given by

$$r(t) = -\ddot{u}_b(t) - \frac{B_f}{\rho_b A_b (1 + C_m)} \dot{u}_b(t) + \frac{\rho_b C_m + \rho_f}{\rho_b (1 + C_m)} \ddot{u}_f(t) + \frac{B_f}{\rho_b A_b (1 + C_m)} \dot{u}_f(t) \tag{13}$$

2.2.2 The First Vibrational Mode. As in previous models of vibrating microscale cantilevers in liquid [28,29,32], the main dynamics can be captured through the first vibrational mode of the cilium. Toward this, the cilium deflection $\hat{w}$ is split into its modal components, with separated spatial X and temporal T parts, as

$$\hat{w}(x,t) = \sum_{n=1}^{\infty} X_n(x) T_n(t) \tag{14}$$

and substituted into Eq. (12) to obtain

$$\sum_{n=1}^{\infty} X_n(x) \ddot{T}_n(t) + \frac{(B_f + B_i)}{\rho_b A_b (1 + C_m)} \sum_{n=1}^{\infty} X_n(x) \dot{T}_n(t) + \frac{EI}{\rho_b A_b (1 + C_m)} \sum_{n=1}^{\infty} X_n''''(x) T_n(t) = r(t) \tag{15}$$

Note that $X_n(x)$ represents the shape of the nth vibrational mode, which is obtained by considering the homogeneous equation with $r(t) = 0$ in Eq. (15). The homogeneous equation is satisfied if each mode satisfies

$$X_n(x) \ddot{T}_n(t) + \frac{(B_f + B_i)}{\rho_b A_b (1 + C_m)} X_n(x) \dot{T}_n(t) + \frac{EI}{\rho_b A_b (1 + C_m)} X_n''''(x) T_n(t) = 0 \tag{16}$$

which can be rewritten as a spatial (position x dependent) function on one side and a temporal (time t dependent) function on the other side that are, hence, both equal to a constant $(-z_n^2)$, i.e.

$$\frac{\ddot{T}_n(t)}{T_n(t)} + \frac{(B_f + B_i)}{\rho_b A_b (1 + C_m)} \frac{\dot{T}_n(t)}{T_n(t)} = -\frac{EI}{\rho_b A_b (1 + C_m)} \frac{X_n''''(x)}{X_n(x)} = -z_n^2$$

This yields two equations for the spatial X_n and temporal T_n portions of the mode

$$\ddot{T}_n(t) + \frac{(B_f + B_i)}{\rho_b A_b (1 + C_m)} \dot{T}_n(t) + z_n^2 T_n(t) = 0 \tag{17}$$

$$X_n''''(x) - \frac{\rho_b A_b (1 + C_m)}{EI} z_n^2 X_n(x) = 0 \tag{18}$$

The mode shape X_n can be obtained from Eq. (18) as [33]

$$X_n(x) = \cosh(\beta_n x) - \cos(\beta_n x) - \sigma_n(\sinh(\beta_n x) - \sin(\beta_n x)) \tag{19}$$

where

$$X_n''''(x) = \beta_n^4 X_n(x) \tag{20}$$

$$\beta_n = \left[\frac{\rho_b A_b (1 + C_m)}{EI} z_n^2\right]^{1/4} \tag{21}$$

For the first mode $(n = 1)$ of vibration, the parameters in the mode shape $(X_1(x)$ in Eq. (19)) can be found from the boundary conditions (in Eq. (3)) as [33]

$$\beta_1 L = 1.875 \quad \text{and} \quad \sigma_1 = 0.7341 \quad \text{and} \quad X_1(L) = 2 \tag{22}$$

Multiplying the nonhomogeneous Eq. (15) with the first mode $X_1(x)$, using the mode shape property in Eq. (20) and integrating with respect to the length dx, results in

$$\sum_{n=1}^{\infty} \int_0^L X_1(x) X_n(x) dx \ddot{T}_n(t) + \frac{(B_f + B_i)}{\rho_b A_b (1 + C_m)} \sum_{n=1}^{\infty} \int_0^L X_1(x) X_n(x) dx \dot{T}_n(t) + \frac{EI}{\rho_b A_b (1 + C_m)} \sum_{n=1}^{\infty} \int_0^L \beta_n^4 X_1(x) X_n(x) dx T_n(t) = r(t) \int_0^L X_1(x) dx$$

The orthogonality of the mode shapes results in only the first mode remaining after the integration in the above equation to yield

$$\ddot{T}_1(t) + \frac{(B_f + B_i)}{\rho_b A_b (1 + C_m)} \dot{T}_1(t) + \frac{EI}{\rho_b A_b (1 + C_m)} \beta_1^4 T_1(t) = r(t) K_1 \tag{23}$$

$$K_1 = \frac{\int_0^L X_1(x) dx}{\int_0^L X_1(x) X_1(x) dx} = \frac{0.783L}{L} = 0.783 \tag{24}$$

which can be rewritten (using the forcing term r from Eq. (13)) as

$$\ddot{T}_1(t) + 2(\zeta_f + \zeta_i)\omega_n \dot{T}_1(t) + \omega_n^2 T_1(t) = 0.783 r(t) \tag{25}$$

where the natural frequency ω_n, fluid damping ratio ζ_f, and internal damping ratio ζ_i are given by

$$\omega_n = \left[\beta_1^2 \sqrt{\frac{EI}{\rho_b A_b}}\right] \frac{1}{\sqrt{(1 + C_m)}} = \frac{\omega_n^*}{\sqrt{(1 + C_m)}} \tag{26}$$

$$\zeta_f = \frac{1}{2\omega_n} \left[\frac{B_f}{\rho_b A_b (1 + C_m)}\right] = \frac{B_f}{2\beta_1^2 \sqrt{EI \rho_b A_b}} \frac{1}{\sqrt{(1 + C_m)}} = \frac{\zeta_f^*}{\sqrt{(1 + C_m)}} \tag{27}$$

$$\zeta_i = \frac{1}{2\omega_n}\left[\frac{B_i}{\rho_b A_b(1+C_m)}\right] = \frac{B_i}{2\beta_1^2\sqrt{EI\rho_b A_b}}\frac{1}{\sqrt{(1+C_m)}} = \frac{\zeta_i^*}{\sqrt{(1+C_m)}} \tag{28}$$

where ω_n^*, ζ_f^*, and ζ_i^* are the natural frequency, fluid damping ratio, and internal damping ratio, respectively, without the added-mass effect. Moreover, the output tip displacement, due to the first vibrational mode X_1 and the base motion $u_b(t)$, is

$$y(t) = X_1(L)T_1(t) + u_b(t) = 2T_1(t) + u_b(t) \tag{29}$$

since $X_1(L) = 2$ (as in Eq. (22)).

2.3 Effect of Sloshing on Cilia Vibration. The effect of the external forcing (chamber oscillation) on the cilia vibration consists of two parts: (i) the direct forcing due to the motion of the chamber (or cilia base u_b) and (ii) the forcing due to fluid motion u_f, which can be different from the chamber/base motion u_b because of fluid sloshing. In particular, these two components (u_b and u_f) arise in the forcing term $r(t)$ (Eq. (13)) and, thereby, appear on the right hand side of the cilium vibration Eq. (25), which can be rewritten in the frequency domain as

$$\begin{aligned}\left[s^2 + 2\zeta_2\omega_n s + \omega_n^2\right]T_1(s) &= 0.783 r(s) \\ &= -0.783\left[s^2 + 2\zeta_1\omega_n s\right]u_b(s) \\ &\quad + 0.783\left[\frac{\rho_b C_m + \rho_f}{\rho_b(1+C_m)}s^2 + 2\zeta_1\omega_n s\right]u_f(s)\end{aligned} \tag{30}$$

where $\zeta_1 = \zeta_f$ and $\zeta_2 = \zeta_f + \zeta_i$. If the chamber motion and the accompanying sloshing amplitude are not too large, then the additional motion of the fluid u_f over the motion of the chamber u_b can be captured using linear models, e.g., Refs. [17,38], such as a second-order model of the form [17]

$$u_f(s) = \frac{-K_{sl}s^2}{s^2 + 2\omega_{sl}\zeta_{sl}s + \omega_{sl}^2}u_b(s) + u_b(s) \tag{31}$$

$$= [G_{sl}(s) + 1]u_b(s) \tag{32}$$

where G_{sl} is the sloshing transfer function that quantifies the additional motion u_f of the fluid (at the level of the cilia in the chamber) over the motion u_b of the chamber, and K_{sl}, ζ_{sl}, and ω_{sl} are the gain, damping ratio, and natural frequency of sloshing in the chamber, respectively. These parameters depend on the fluid properties, the geometry of the chamber, and the height of the cilia location from the base of the chamber.

Note that if there is no sloshing, then displacement of the fluid u_f is equal to that of the chamber u_b . In that case, the sloshing gain K_{sl} is zero, e.g., at the base of the chamber. Similarly, at a low frequency ω, the amplification factor $|G_{sl}|_{s=j\omega}$ of the sloshing transfer function G_{sl} tends to be small due to the s^2 term in the numerator and the fluid motion u_f becomes close to the chamber motion u_b .

2.3.1 Transfer Function Model. The vibrational response of the cilium's tip y (in Eq. (29)) can be rewritten using the sloshing dynamics (in Eq. (32)) and the cilium vibrational model (in Eq. (30)) as

$$\frac{y(s)}{u_b(s)} = G_y(s) = 2\frac{T_1(s)}{u_b(s)} + 1 \tag{33}$$

$$= G_1(s) + G_{sl}(s)G_2(s) + 1 \tag{34}$$

where

$$G_1(s) = 1.566\frac{\dfrac{(\rho_f - \rho_b)}{\rho_b(1+C_m)}s^2}{s^2 + 2\zeta_2\omega_n s + \omega_n^2} \tag{35}$$

$$G_2(s) = 1.566\frac{\dfrac{\rho_b C_m + \rho_f}{\rho_b(1+C_m)}s^2 + 2\zeta_1\omega_n s}{s^2 + 2\zeta_2\omega_n s + \omega_n^2} \tag{36}$$

This completes the theoretical modeling of the cilia-motion dynamics.

3 Experimental Results and Discussions

Experimental data in this section is used to highlight the need to capture the added-mass effect and the sloshing effect in the theoretical model developed in Sec. 2. Additionally, issues that affect the amplitude of cilia motion, such as the liquid height and cilia length, are investigated experimentally. Finally, it is shown that cilia can be used to achieve faster mixing by comparing mixing results with and without cilia.

3.1 Added-Mass and Sloshing Effects on Cilia Response. The following experimental results show the importance of including both the added-mass effect and the sloshing effect to capture the frequency response of the cilia. Toward this, the frequency responses of cilia are comparatively evaluated for three cases as illustrated in Fig. 3. In the first case (a), the cilia are oscillated in air as in Fig. 3(*a*). In the second case (b), the same cilia (as in case (a)) are oscillated in de-ionized (DI) water to comparatively evaluate the effect of moving the cilia in a dense fluid (water) instead of air. In this second case, the chamber containing the water is stationary—therefore, sloshing is not present. In the final case (c), the entire chamber is oscillated (which leads to liquid sloshing) to comparatively evaluate the cilia dynamics with and without sloshing. All the cilia in the three sets of experiments have identical dimensions.

3.1.1 Experimental Frequency Response Data. The frequency response of the cilia dynamics is obtained by varying the frequency of oscillation. The amplitude of the piezoactuator's motion, which generates cilia oscillation (in cases (a) and (b)) and the chamber/cilia oscillation (in case (c)), is kept fixed at 10 μm for all the three sets of experiments. The amplitudes of the cilia-tip motion y and the cilia-base motion u_b are measured from images obtained from the video camera. The experimentally obtained frequency responses for the three cases are shown in Fig. 4. Each data point in these figures represents the average amplification, of the cilia motion y over the base motion u_b, of the three cilia in each experimental run.

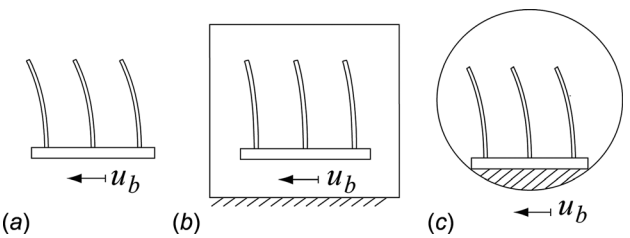

Fig. 3 Schematic experimental setup (images not to scale) for evaluating the effects of added mass and sloshing on the frequency response of cilia. Case (*a*) the cilia are oscillated in air; case (*b*) the cilia are oscillated in water (inside a stationary, relatively large 60 mm × 115 mm chamber); and case (*c*) the chamber (3 mm diameter) containing the cilia is oscillated. In each case, three cilia are used.

Table 1 Parameters for three cilia (length $L = 800$ μm) actuated in air, i.e., case (a), with the transfer function given in Eq. (37). The resonance frequency of the fitted model is $\omega_{r,a}$.

Case (a)	$\zeta_{1,a}$	$\zeta_{2,a}$	$\omega_{n,a}$ (Hz)	$\omega_{r,a}$ (Hz)
Cilium 1	0.149	0.166	335.84	333.27
Cilium 2	0.149	0.165	338.11	335.52
Cilium 3	0.151	0.167	336.26	333.61
Mean	0.150	0.166	336.74	334.13

3.1.2 Model Parameters for Cases (a) and (b). When the cilia are oscillated in a stationary fluid (as in cases (a) and (b)), the nominal velocity of the fluid is set to zero ($u_f = 0$ in Eq. (30)) and the system transfer G_y^* becomes, from Eqs. (30) and (33)

$$\frac{y(s)}{u_b(s)} = G_y^*(s) = 2\frac{T_1(s)}{u_b(s)} + 1 = -1.566\frac{s^2 + 2\zeta_{1,i}\omega_{n,i}s}{s^2 + 2\zeta_{2,i}\omega_{n,i}s + \omega_{n,i}^2} + 1 \quad (37)$$

where the subscript i is either a or b to denote the two cases ((a) or (b)). The model parameters (damping $\zeta_{1,i}, \zeta_{2,i}$ and natural frequency $\omega_{n,i}$) for cilia oscillated in air (case a, $i = a$) and in water (case (b), $i = b$) were obtained by minimizing the least-square of the error between the experimental and predicted frequency responses for each cilium. The parameters obtained through this fit of the experimental data are provided in Table 1 for case (a) and in Table 2 for case (b). It is noted that the parameters (in Tables 1 and 2) are similar for the different cilia in each experimental run. The resulting frequency responses predicted by the models (using the mean values in Tables 1 and 2 for cases (a) and (b)) are shown in Fig. 4.

3.1.3 Effect of Added Mass on Frequency Response of Cilia. The added-mass effect leads to a substantial reduction in the resonant-vibrational frequency in water, $\omega_{r,b}$, when compared to air (for the same set of three cilia) as seen in Fig. 4 and in Tables 1 and 2. In particular, the mean resonant-vibrational frequency in water $\omega_{r,b} = 110.14$ Hz (Table 2) is substantially lower than the mean resonant-vibrational frequency in air $\omega_{r,a} = 334.13$ Hz (Table 1). Damping effects (in water as opposed to air) cannot explain the substantial reduction in the resonant-vibrational frequency of the cilia oscillated in water when compared to the cilia oscillated in air. For example, a standard second-order model for cantilever structures would yield a resonant-vibrational frequency expression of

$$\omega_{r,w} = \omega_{n,a}\sqrt{1 - 2\zeta^2} \quad (38)$$

where ζ is the damping ratio (e.g., see Ref. [39], Sec. 10.8).

With a damping ratio ζ in water ranging from 0.05 to 0.5 (e.g., Ref. [28]), the anticipated, resonant-vibrational frequency $\omega_{r,b}$ in a water is expected to be between $0.997\omega_{n,a} = 335.73$ Hz and $0.707\omega_{n,a} = 238.08$ Hz from Eq. (38). Note that this range for the anticipated, resonant-vibrational frequency (from 238.08 to 335.73 Hz) is much larger than the mean, resonant-vibrational frequency in water from experiments of $\omega_{r,b} = 110.14$ Hz (Table 2). Thus, damping alone is not sufficient to capture the substantial reduction in the resonant vibrational frequency of cilia actuators when oscillated in liquids when compared to oscillation in air.

Table 2 Parameters for three cilia (the same cilia as in Table 1 in air) actuated in water, i.e., case (b), with the transfer function given in Eq. (37). The resonance frequency of the fitted model is $\omega_{r,b}$.

Case (b)	$\zeta_{1,b}$	$\zeta_{2,b}$	$\omega_{n,b}$ (Hz)	$\omega_{r,b}$ (Hz)
Cilium 1	0.441	0.457	115.08	107.74
Cilium 2	0.442	0.451	120.16	112.80
Cilium 3	0.432	0.446	116.95	109.87
Mean	0.438	0.451	117.40	110.14

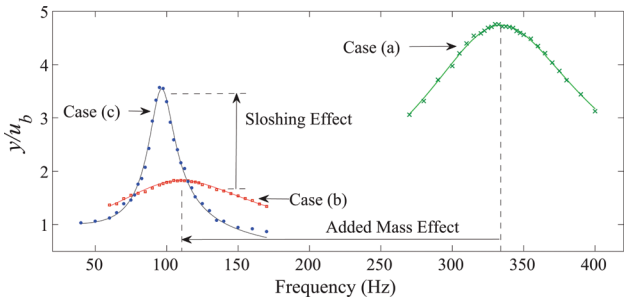

Fig. 4 Frequency responses for three cases. The frequency responses of the fitted models are shown using solid lines, and experimental mean values (for three cilia in each case) are represented by dots. Case (a) the cilia are oscillated air; case (b) the cilia are oscillated in water (inside a stationary chamber); and case (c) the chamber containing the cilia is oscillated. The same set of cilia is used in case (a) and case (b) to capture the added-mass effect. The estimated added mass is used to model the cilia response with sloshing in case (c).

The added-mass effect (that accounts for the inertial loading of the fluid) can account for the substantial reduction in the resonant vibrational frequency when operating cantilever-type devices in liquids [32]. Note that the mean, natural frequency in water $\omega_{n,b} = 117.40$ Hz (Table 2) is substantially lower than the mean, natural frequency in air $\omega_{n,a} = 336.74$ Hz (Table 1). The natural frequency should not be affected by the fluid damping and can be used to estimate the added-mass coefficient C_m from Eq. (26) as

$$C_m = \left[\frac{\omega_n^{*2}}{\omega_{n,b}^2} - 1\right] \approx \left[\frac{\omega_{n,a}^2}{\omega_{n,b}^2} - 1\right] = \left[\frac{336.74^2}{117.40^2} - 1\right] = 7.23 \quad (39)$$

where the added-mass effect in air (which has low density compared to water) is neglected. By increasing the effective mass (due to the need to accelerate the surrounding fluid), the model with the added mass has a substantially lower natural frequency (as in Eq. (26)) and, thereby, captures the substantially lower resonant-vibrational frequency [32]. This value 7.23 for the added-mass coefficient is used in the rest of the article since all cilia, used in the experiments, are made from the same silicon mold using the same fabrication procedures.

3.1.4 Effect of Sloshing on Frequency Response of Cilia. The model parameters (in Eq. (31)) for the liquid sloshing, obtained by minimizing the least-square of the error between the model's predicted frequency response and the mean experimental frequency response in Fig. 4, are given by

$$K_{sl} = 0.489, \quad \zeta_{sl} = 0.095, \quad \omega_{sl} = 96.63\text{Hz} \quad (40)$$

When finding the sloshing parameters, the cilia-related terms (G_1, G_2) in the dynamics G_y (Eq. (34)) were kept the same as the mean values for case (b) in Table 2 when the cilia were oscillated in a stationary chamber, i.e.

$$\zeta_1 = 0.438, \quad \zeta_2 = 0.451, \quad \omega_n = 117.40\text{Hz}, \quad C_m = 7.23 \quad (41)$$

Moreover, the density of the water is $\rho_f = 1000$ kg/m^3 and the density of the PDMS cilium is $\rho_b = 950$ kg/m^3. The resulting

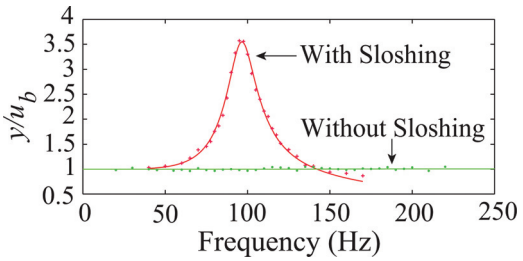

Fig. 5 Experimental frequency responses (mean value of three cilia) with and without sloshing, i.e., free surface is constrained from sloshing with a glass cover. The same set of three cilia was used for both experiments, with and without sloshing.

frequency response predicted by the model for case (c) with the parameters in Eqs. (40) and (41) is shown in Fig. 4. It is noted that there is a substantial increase in the cilia motion with sloshing (i.e., when the chamber is oscillated) when compared to the case (b) when the chamber is stationary.

To summarize, both, the sloshing effect and the added-mass effect are important when modeling the cilia dynamics—the added mass reduces the natural frequency ω_n of the cilia vibration (compare cases (a) and (b) in Fig. 4) and sloshing increases the amplitude of cilia motion (compare cases (b) and (c) in Fig. 4).

3.2 Experimental Study of Sloshing Dynamics. The importance of sloshing dynamics to achieve large amplitude cilia motion is studied in this subsection by comparatively evaluating the cilia motion with and without sloshing for the oscillating chamber (case (c)). Additionally, the effect of liquid height on the sloshing dynamics (and therefore the cilia motion) is experimentally investigated.

3.2.1 Response With and Without Sloshing for Oscillating Chamber. Sloshing is important to generate the large-amplitude, cilia motion when the entire chamber is oscillated (case (c)). To illustrate this, sloshing was experimentally suppressed by using a glass slide to cover the chamber (which is filled with DI water) and thereby constraining the sloshing of the water surface. The response of the same set of cilia, with and without the glass-slide cover, i.e., without and with sloshing, is shown in Fig. 5. Note that the amplitude of cilia motion is substantially reduced when sloshing is suppressed as opposed to the case when the water surface is free to slosh. When sloshing is suppressed, the sloshing gain K_{sl} in the transfer function G_y (see Eqs. (31) and (34)) becomes close to zero.

3.2.2. Cilia Motion Without Sloshing. Even without sloshing, vibrational resonance could lead to large-amplitude, cilia motion when the entire chamber is oscillated (case (c)). However, such large amplitudes should not be expected, as discussed below. Note that the dynamics of the cilia motion without sloshing ($G_{sl} = 0$ in Eq. (34)) reduces to the term G_1 in the transfer function in Eq. (34). The numerator of this term G_1 contains the difference between the density of the liquid ρ_f and the density of the cilium ρ_b, which implies that the transfer function gain tends to zero when the two densities become close. In the current experimental system, the two densities are close—the density of the water is $\rho_f = 1000$ kg/m^3 and the density of the PDMS cilium is $\rho_b = 950$ kg/m^3. Therefore, the amplification of the cilia motion due to cilia resonance without sloshing, represented by the term G_1, is small. This implies that the cilia and the fluid tend to move together with the chamber when the chamber is oscillated without sloshing. Thus, large cilia motion is not achieved without sloshing, and therefore sloshing plays an important role in achieving large cilia motion as illustrated by the experimental results in Fig. 5.

3.2.3 Effect of Liquid Height on Cilia Dynamics. The sloshing dynamics, modeled by a linear second order system in Eq. (31), depends nonlinearly on the geometric properties of the chamber such as its diameter and the liquid height. For example, the variation of the frequency response when the liquid height is varied for the same set of cilia is shown in Fig. 6. As the liquid height increases, the distance of the cilia (which is at a fixed height from the base of the chamber) from the free surface of the sloshing water also increases. The sloshing parameters corresponding to each height experiment are obtained by minimizing the least-square of the error between the model's predicted frequency response and the mean experimental frequency response in Fig. 6, where the cilia-related terms (G_1, G_2) in the dynamics G_y (Eq. (34)) were kept the same as the mean values for case (b) given in Eq. (41). The resulting sloshing parameters are given in Table 3.

The variation in the sloshing response with different liquid heights in the chamber, which also changes the distance of the cilia from the free surface, is expected. In particular, the liquid near the free surface has a larger sloshing amplitude compared to the liquid farther below the free surface [17]. Therefore, the sloshing gain K_{sl} is expected to decrease with an increase in the liquid height above the cilia. Moreover, the reduction in the sloshing natural-frequency ω_{sl} in Table 3 with liquid height is also expected in standard sloshing models, which predict that the sloshing natural-frequency, for cylindrical containers, is proportional to the square root of a hyperbolic tangent function of the depth of water [17]. Although standard sloshing models are developed for

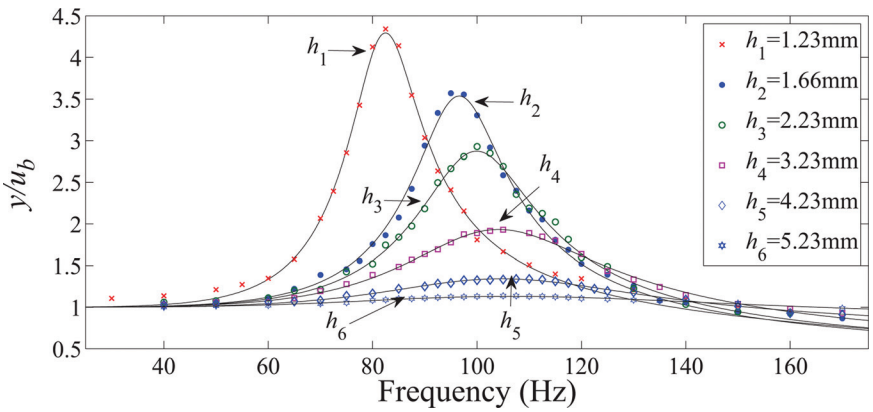

Fig. 6 Frequency responses for cilia in an oscillating chamber when the height of water is varied. Each data point (dot) represents the average value for the three cilia used in each experiment. The same cilia are used in all these experiments. The frequency responses of the fitted models are given by solid lines.

Table 3 Variation of sloshing parameters with water height in the chamber

Water level h (mm)	ω_{sl} (Hz)	ζ_{sl}	K_{sl}
$h_1 = 1.23$	82.26	0.085	0.631
$h_2 = 1.66$	96.63	0.095	0.489
$h_3 = 2.23$	100.11	0.119	0.448
$h_4 = 3.23$	104.67	0.198	0.376
$h_5 = 4.23$	106.41	0.287	0.209
$h_6 = 5.23$	107.23	0.471	0.136

relatively larger containers [17], the sloshing in the chamber has a similar functional dependence on the liquid height in the range of the operating conditions. In particular, the natural frequency variation with height, in Table 3 and shown in Fig. 7, has the form

$$\omega_{sl}^2 = \frac{A}{(2\pi)^2}\left[\tanh\left(B\frac{h}{R}\right)\right] \tag{42}$$

where h is the water level, R is the radius of the chamber, ω_{sl} is the sloshing natural frequency in Hertz, and with the least-squares fit to reduce the error between the model and the experimental values resulting in parameters

$$A = 454460, \quad B = 0.9$$

The resulting prediction of the variation in the sloshing natural-frequency in Eq. (42) is shown in Fig. 7, which indicates that the frequency-variation with liquid-height meets the expected hyperbolic tangent relation. It is noted that such models can be used to predict the sloshing frequencies for other water levels in the chamber, e.g., to optimize the interaction between the cilia dynamics (G_2 term in Eq. (34)) and the sloshing dynamics (G_{sl} term in Eq. (34)) for maximizing the cilia response.

3.3 Fluid-Structure Interaction. The interaction between the liquid dynamics (sloshing) and the structural dynamics (cilia vibrations) predicted by the model is experimentally investigated in this subsection.

3.3.1 Fluid-Structure Interaction in the Model. For a given sloshing dynamics ($K_{sl}, \zeta_{sl}, \omega_{sl}$), the cilia motion will be excited the most when the cilia resonance $\omega_{r,b}$ in water gets close to the sloshing natural frequency ω_{sl} . This is because the increase in the cilia motion y compared to the chamber oscillation u_b depends on the product $G_{sl}G_2$ (in Eq. (34))—especially since the term G_1 is small when the liquid density ρ_f is close to the cilia density ρ_b as discussed before. The product $G_{sl}G_2$ becomes large when each term becomes large. More precisely, the cilia-motion amplitude will be maximized when the resonance frequency of the structural-vibration term G_2 is the same as the resonance frequency of the sloshing term G_{sl} and the cilia motion will be maximized if both these resonance frequencies (of structural-vibrations G_2 and sloshing G_{sl}) are the same. Thus, the interaction of the sloshing dynamics (G_{sl} term) with the structural-vibration dynamics (G_2 term) is important in determining the cilia motion.

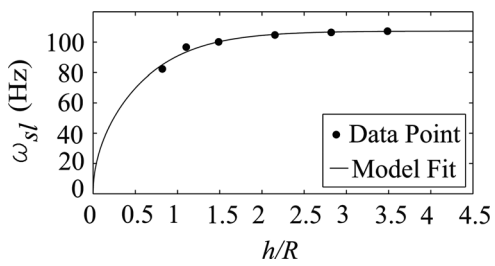

Fig. 7 Variation of the sloshing natural-frequency ω_{sl} with the ratio of the water height h to the chamber radius R. The dots represent the experimental data and the solid line represents the prediction by the fitted model in Eq. (42).

3.3.2 Interaction of Sloshing and Added-Mass Effects. The added-mass effect plays a key role in the interaction between structural-vibrational resonance and sloshing resonance by lowering the vibrational-resonance frequency. For example, without the added-mass effect, the resonance frequency would be at 334.13 Hz (see Table 1). The ensuing excitation of structural vibrations by sloshing with such a high vibrational-resonance frequency (without the added-mass effect) would not be as much as the case when the vibrational-resonance frequency of the cilia is lowered by the added-mass effect. This re-emphasizes the importance of considering both effects, added-mass and sloshing, to capture the response of the cilia.

3.3.3 Experimental Results for Varying Cilia Length. For a given sloshing response, increased cilia motion should be expected when the natural frequency of the cilia in water ω_n gets closer to the natural frequency ω_{sl} of the sloshing dynamics—note that the resonance frequencies are close to the natural frequencies due to small damping. To illustrate this, the frequency responses of cilia with different lengths (i.e., different vibrational response G_2 and natural frequencies) are excited with the same sloshing dynamics G_{sl}, i.e., a fixed natural frequency for sloshing. One expects the motion to be largest for cilia whose resonance frequency of structural vibration is closest to the resonance frequency of sloshing.

3.3.3.1 Procedure and results. Cilia were cut with a sharp blade, and the lengths were measured using images acquired with the microscope where the length of the uncut cilia is known a priori. The frequency responses of the different-length cilia were measured when the cilia were oscillated in a stationary chamber (case (b)) and when the chamber was oscillated (case (c)). The same cilia were used in both the experiments. The experimental frequency responses for each case (shown in Fig. 8 and 9) were fitted using least-squares error minimization as discussed before (for cases (b) and (c)) and the resulting model parameters are shown in Tables 4 and 5.

3.3.3.2 Discussion of length effect. As anticipated, when the chamber is oscillated, the sloshing tends to excite the cilia substantially more if the sloshing resonance is close to the cilia resonance. For example, the 800 μm cilium has the largest amplitude (seen in Fig. 9 as well as Table 5) because its vibrational-resonance frequency in water $\omega_{r,w} = 108.40$ Hz (see Table 4) is closest to the sloshing resonance-frequency that is, in turn, close to the sloshing natural-frequency ω_{sl} that lies between 95 and 98 Hz (see Table 5). Note that even with different lengths, the maximum (input-to-output) amplifications of the different-length cilia are about the same when the cilia are oscillated in the fixed chamber—see Fig. 8 and Table 4—the shortest 425 μm cilium has a maximum amplification A_{max} of 1.75, which is close to the maximum amplification of 1.85 for the longest 800 μm cilium in Table 4. In contrast, the amplification ratios are substantially lower for the two, shorter cilia than the longest cilium in the sloshing case—the shortest 425 μm cilium has a maximum amplification of 1.83, which is much smaller than the maximum amplification of 3.58 for the longest 800 μm cilium in Table 5.

3.3.3.3 Predictive capabilities of the model. The model can predict the variation in the dynamics with the change in length, e.g., for the cut cilia. To illustrate, the parameters found for the intact (not cut) 800 μm cilium were used to predict the response of cut cilia in the oscillating chamber. In particular, the natural

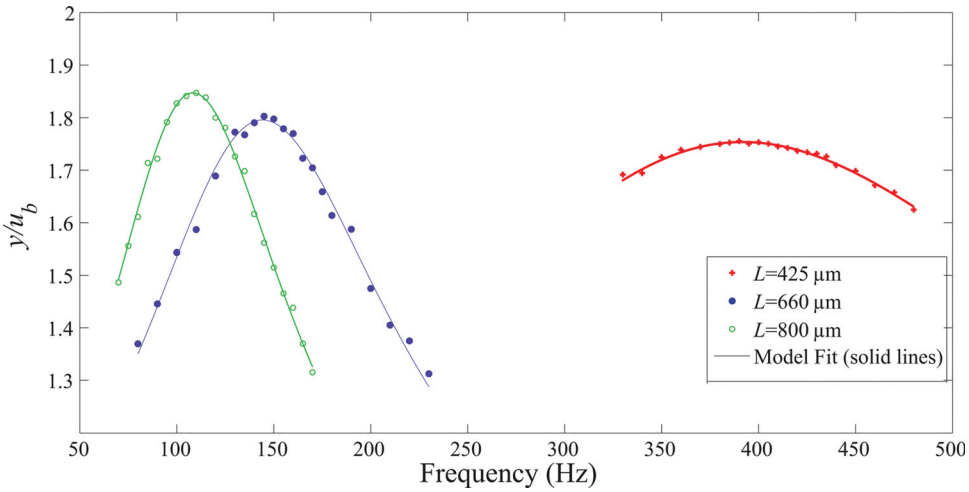

Fig. 8 Stationary chamber (case (b)): frequency responses for different-length cilia. Experimental values are represented by dots. Responses of models with parameters fitted by least-squares error minimization is presented with solid lines.

frequencies of the shorter cilia (in a stationary chamber) were predicted as

$$\omega_{n,w,660} = \omega_{n,w,800} * (800/660)^2 = 169.46\text{Hz}$$
$$\omega_{n,w,425} = \omega_{n,w,800} * (800/425)^2 = 408.68\text{Hz} \quad (43)$$

since the natural frequency of a vibrating cantilever is inversely proportional to the square of the length, where the lengths of the cilia are added as subscripts for clarity. The damping ratios (ζ_1, ζ_2) do not change significantly with length (as seen in Table 4 as well as in previous work [32]); therefore, the damping ratios for the cut cilia were chosen to be the same as the damping ratios for the uncut 800 μm cilium, i.e., $\zeta_1 = 0.435$ and $\zeta_2 = 0.446$ from Table 4. The sloshing parameters in the predicted models for the cut cilia were kept the same as those for the uncut 800 μm cilium, i.e., $K_{sl} = 0.482$, $\zeta_{sl} = 0.094$, $\omega_{sl} = 97.07$ from Table 5.

The predicted frequency response is close to the frequency response of the fitted models and the experimental data of the frequency response as shown in Fig. 9. The maximum errors E_{fit}, E_{pred} in the frequency response between the fitted and predicted models, provided in Table 5, are defined as

$$E_{\text{fit}} = \max_{\omega_k} \left| \frac{A_{\text{fit}}(\omega_k) - A_{\text{exp}}(\omega_k)}{A_{\text{exp}}(\omega_k)} \right| \times 100,$$
$$E_{\text{pred}} = \max_{\omega_k} \left| \frac{A_{\text{pred}}(\omega_k) - A_{\text{exp}}(\omega_k)}{A_{\text{exp}}(\omega_k)} \right| \times 100 \quad (44)$$

where A_{exp}, A_{fit}, and A_{pred} represent the amplification factors of the frequency responses (at each frequency ω_k where the experimental data are available) from the experiments, fitted models, and predicted models, respectively. Note that the maximum error E_{pred} with the predicted model (e.g., 9.12 for the 660 μm cilium) is similar to the maximum error E_{fit} of the fitted model, e.g., 6.46 for the 800 μm cilium that is used to predict the model of the cut cilia. Hence, the model can be used to evaluate the effect of changing cilia length. For example, with a given chamber geometry (i.e., given sloshing dynamics), the model could be used to optimize the cilia length for maximizing the cilia motion.

The validity of using the above models for predicting the effect of parameter variations such as cilia stiffness and fluid viscosity has not been investigated in this work. For example, previous work [17] (pages 166–167) has shown that the main sloshing frequency tends to be relatively insensitive to large changes in fluid

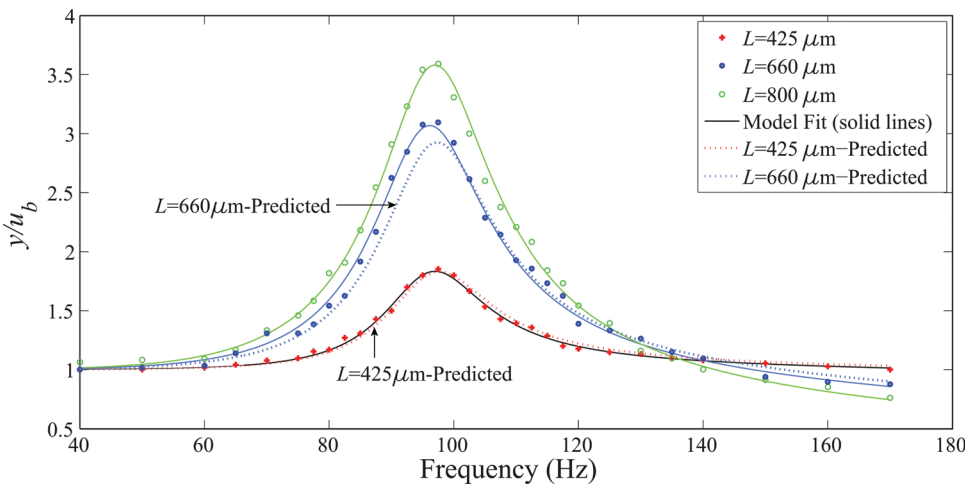

Fig. 9 Oscillating chamber (case (c)): frequency responses for different-length cilia. Experimental values are represented by dots. Response of models with parameters fitted by least-squares error minimization is presented with solid lines. Dashed lines represent responses of predicted models.

Table 4 Stationary chamber: parameters and maximum amplification A_{max} of fitted models for different-length cilia corresponding to Fig. 8

$L(\mu m)$	ζ_1	ζ_2	$\omega_{n,w}$ (Hz)	$\omega_{r,w}$ (Hz)	A_{max}
425	0.458	0.472	420.42	391.68	1.75
660	0.443	0.459	154.21	144.28	1.80
800	0.435	0.446	115.34	108.40	1.85

viscosity. Nevertheless, such studies were for relatively large-sized chambers. Additional work is needed to validate the currently proposed models for such parameter variations.

3.4 Mixing With and Without Cilia. The mixing results of ink and water in an oscillating chamber with-and-without cilia (but with liquid sloshing in each case) are comparatively evaluated to show that the use of cilia leads to faster mixing.

3.4.1 Procedure for Mixing Experiments. The procedure of the mixing experiment with cilia is described below. The procedure for the mixing experiments without cilia (i.e., vibration only) is the same as the case with cilia except that cilia are not present in the chamber. For mixing experiments with cilia, three cilia are arranged in the mixing chamber as shown in Fig. 10. The cilia mixing device is attached to the piezoactuator as shown in Fig. 1(*a*). The cilia mixer system is positioned above an inverted microscope. After positioning the cilia mixer, DI water (11 μl) is added to the chamber using a pipette. Collapsed cilia, if any, are straightened by using tweezers. Next, 0.25 μl of black ink (Drawing ink A, Pelikan, Hannover, Germany, that is diluted 80 times with DI water) is released gently using a pipette at the center of the chamber under the water surface. The initial image of the ink drop (at time $t = 0$ s) is shown in Fig. 11. A thin PDMS sheet is placed above the chamber to enclose the mixing chamber to avoid evaporation of the solution during the mixing experiments. The PDMS cover does not suppress sloshing of the free surface because the solution volume together with the cilia-support structure creates a maximum water height of 1.66 mm, which does not reach the top of the chamber. Additionally, a support for the cover is added (as in Fig. 10) to prevent the cover from sagging and touching the water surface. Subsequently, the piezoactuator is used to oscillate the chamber perpendicular to the length of the cilia with an amplitude of 10 μm as in Fig. 3(*c*). The oscillation frequency is chosen as the maximum-amplitude resonance frequency with the cilia, which was measured for each run before the ink was introduced—this oscillation frequency is kept the same for both cases, with and without cilia, for that particular run.

Each mixing experiment (with and without cilia) was repeated seven times. For each mixing experiment, the initial image is captured after the addition of ink and after the thin PDMS sheet is used to cover the chamber but just before the start of the chamber oscillations with the piezoactuator. Preliminary experiments were performed to choose a sufficiently large time for the mixing experiments such that the mixing index (described in the section below) reaches a steady state value. Based on these preliminary

Table 5 Oscillating chamber: parameters and maximum amplification A_{max}, of fitted models for different-length cilia corresponding to Fig. 9 along with maximum error (Eq. (44)) in fitted and predicted models.

(μm)	ζ_{sl}	ω_{sl} (Hz)	K_{sl}	$A_{\max}$	E_{fit}	E_{pred}
425	0.093	96.47	0.478	1.83	3.70	5.36
660	0.095	95.98	0.492	3.07	4.82	9.12
800	0.094	97.07	0.482	3.58	6.46	N/A

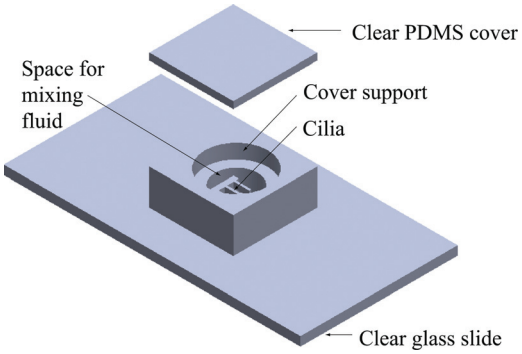

Fig. 10 Schematic setup of cilia device shown in Fig. 1(*a*) for mixing experiments in a 3 mm diameter chamber

studies, the time t_N for the final image was chosen as 50 s for the case with cilia and 600 s for the case without cilia. (Additionally, the images were inspected to visually verify that they do not change significantly when the last images were collected.) The time for the mixing index to reach and stay within 90% of its final value is used to quantify and comparatively evaluate the mixing performance with and without cilia. A CCD camera, attached to the microscope (see Fig. 1(*a*)), is used to videorecord the mixing process for evaluation; samples of the acquired images are shown in Fig. 11.

3.4.2 Quantifying Mixing. The mixing was quantified by comparing images from the video recording of the mixing process using a mixing index I_{mix} developed in Ref. [40], which is a discrete version of the continuous time mixing index defined in Ref. [41]. The mixing index, which is a measure of relative mixing is initially 0 and approaches 1 when the fluids become fully mixed, is given by

$$I_{\text{mix}}(t_k) = \frac{1}{I_{ss}}\left[1 - \frac{\sum_{p=1}^{P} |C_p(t_k) - C_p(t_N)|}{\sum_{p=1}^{P} |C_p(t_0) - C_p(t_N)|}\right] \tag{45}$$

where $[t_k]_{k=1}^{N}$ represents the different time instants when the images are evaluated, N is the total number of images, P is the number of pixels in each of the images, $C_p(t_k)$ is the color of pth pixel at time instant t_k and the normalization factor I_{ss} is given by

$$I_{ss} = \left|1 - \frac{\sum_{p=1}^{P} |C_p(t_{N-1}) - C_p(t_N)|}{\sum_{p=1}^{P} |C_p(t_0) - C_p(t_N)|}\right|. \tag{46}$$

Each image used in this analysis is composed of an array of 352 pixels by 240 pixels, and the color of each pixel C is a vector of three values

$$C = [R\ G\ B]$$

which represents red, green, and blue color with values between 0 and 255. Given any two pixel colors C_i and C_j, the difference between them (used in Eqs. (45) and (46)) is defined as

$$|C_i - C_j| = |R_i - R_j| + |G_i - G_j| + |B_i - B_j|$$

As the mixing progresses and reaches a steady state (i.e., as t_k approaches t_N), the difference between the color of the corresponding pixels in the images becomes small, which tends to increase the values of I_{mix} from an initial value of zero toward one. The normalization factor I_{ss} in Eq. (46) uses the last two images to make the mixing index close to one when the mixing process reaches steady state and the images become similar. This is necessary because noise in the image (partly due to the

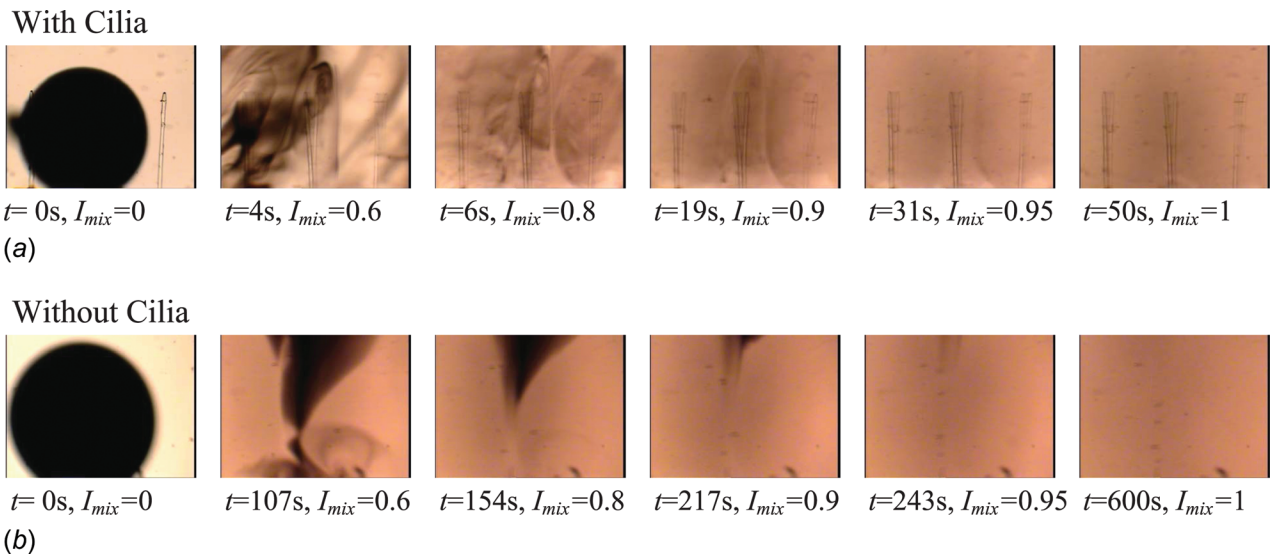

Fig. 11 Sample images of the mixing process at different time instants t and corresponding mixing indices, I_{mix}, as in Eq. (45): (*a*) with cilia, run 1 in Table 6; and (*b*) without cilia, run 1 in Table 6

oscillation) prevents the final value from reaching one without the normalization, i.e., when $I_{ss} = 1$ in Eq. (45).

3.4.3 Mixing Results and Discussions. The mixing time is substantially reduced with cilia when compared to the case without cilia even though liquid sloshing occurs in both cases. The reduction in mixing time is visually observable in the images (with and without cilia) shown in Fig. 11. For example, to reach the 90 % mixing time (corresponding to the images on the fourth column), the mixing takes 19 s with the cilia whereas it takes 217 s for the case without the cilia. To quantify the mixing rate, the variation of the mixing index for the seven experimental runs (with and without cilia) are shown in Fig. 12 and 13 and the 90 % mixing times for the different experiments are presented in Table 6. It is noted that the average mixing time of 14.9 s with cilia is about 12 times lower than the average mixing time of 176.4 s without cilia. Therefore, the use of cilia can substantially decrease the mixing time, by more than one order of magnitude, when compared to the case without cilia. The mixing performance could be improved further with the use of more general inputs (chamber oscillations); the current model (with its relatively low-order dynamics) is well suited for controller development in such future studies.

3.4.4 Potential Use of Model in Mixing Optimization. The current work shows that large cilia motion can be used to reduce the time needed for mixing. The experiments used sinusoidal excitation of the chamber; however, it is possible that a more general input (oscillation of chamber) can lead to even faster mixing. The low order of the current model makes it well suited to design such optimal control for the mixing process. Moreover, by providing insight into effects, such as the interaction between added mass and sloshing in determining cilia motion amplitudes, the model can be used to provide guidelines for optimizing the cilia design, such as the choice of the cilia length for a given chamber geometry. An advantage of the current model is the low order of the dynamics, which does not pose substantial computational burden in optimization studies and controller development. Further work is needed to evaluate these models for such control and design approaches to optimize cilia-based devices.

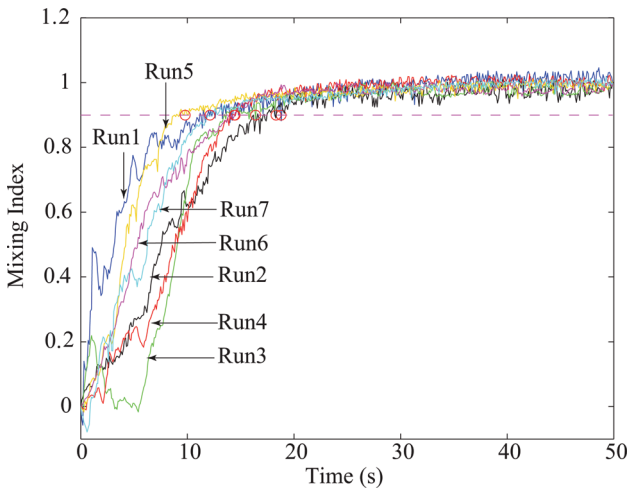

Fig. 12 Time profiles of the mixing index I_{mix} in Eq. (45) for seven experimental runs with cilia. The 90% mixing time is indicated with circles.

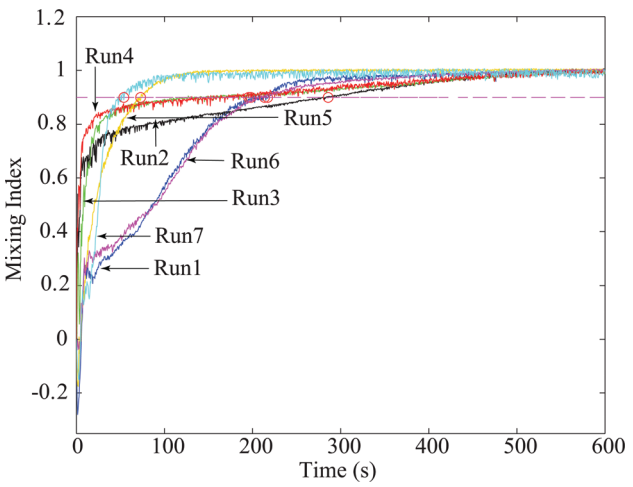

Fig. 13 Time profiles of the mixing index I_{mix} in Eq. (45) for seven experimental runs without cilia. The 90% mixing time is indicated with circles.

Table 6 Mixing time(s) quantified by the time for the mixing index I_{mix} in Eq. (45) to reach and stay within 90% of its final value, with and without cilia

Run number	Oscillation frequency (Hz)	Mixing time with cilia (s)	Mixing time without cilia (s)
1	95	18.8	217
2	97	18.3	285.5
3	96	16.4	193.5
4	96	14.5	198
5	98	9.8	73
6	95	14.4	213.5
7	98	12.1	54
Mean	96.43	14.9	176.4
σ	1.27	3.248	83.02

4 Conclusions

This article modeled the dynamics of cilia-based devices for mixing and manipulating liquids in microfluidic applications. The models showed that, both, sloshing and added-mass effects play substantial roles in generating large-amplitude cilia motion in liquid. Additionally, experimental results, with and without cilia, were comparatively evaluated to show more than one order-of-magnitude reduction in the mixing time with the use of cilia.

Acknowledgment

This work was funded by the National Science Foundation Grant No. CMII 0624597.

References

[1] Miller, C. E., 1968, "The Kinematics and Dynamics of Ciliary Fluid Systems," J. Exp. Biol., **49**, pp. 617–629.
[2] Sleigh, M. A., 1974, *Cilia and Flagella,* Academic, New York .
[3] Brennen, C., 1974, "An Oscillating-Boundary-Layer Theory for Ciliary Propulsion," J. Fluid Mech., **65**(4), pp. 799–824.
[4] Tuck, E. O., 1968, "A Note on a Swimming Problem," J. Fluid Mech., **31**, pp. 305–308.
[5] Ramia, M., Tullock, D. L., and Phanthien, N., 1993, "The Role of Hydrodynamic Interaction in the Locomotion of Microorganisms," Biophys. J., **65**, pp. 755–778.
[6] Gueron, S., and Levit-Gurevich, K., 1998, "Computation of the Internal Forces in Cilia: Application to Ciliary Motion, the Effects of Viscosity, and Cilia Interactions," Biophys. J., **74**, pp. 1658–1676.
[7] Bovender, C. R., 1977, "Nasal Filter," U.S. Patent No. 4052983.
[8] Ataka, M., Omodaka, A., Takeshima, N., and Fujita, H., 1993, "Fabrication and Operation of Polyimide Bimorph Actuators for a Ciliary Motion Ssystem," J. Microelectromech. Syst., **2**(4), pp. 146–150.
[9] Chen, Z., Shatara, S., and Tan, X. B., 2010, "Modeling of Biomimetic Robotic Fish Propelled by an Ionic PolymerMmetal Composite Caudal Fin," IEEE/ASME Trans. Mechatron., **15**(3), pp. 448–459.
[10] Behkam, B., and Sitti, M., 2006, "Design Methodology for Biomimetic Propulsion of Miniature Swimming Robots," ASME J. Dyn. Syst. Meas. Control, **128**(1), pp. 36–43.
[11] Alvarado, P. V. Y., and Youcef-Toumi, K., 2006, "Design of Machines With Compliant Bodies for Biomimetic Locomotion in Liquid Environments," ASME J. Dyn. Syst. Meas. Control, **128**(1), pp. 3–13.
[12] Saif, M. T. A., Alaca, B. E, and Sehitoglu, H., 1999, "Analytical Modeling of Electrostatic Membrane Actuator for Micro Pumps," IEEE J. Microelectromech. Syst., **8**(3), pp. 335–345.
[13] Oh, K., Chung, J.-H., Devasia, S., and Riley, J. J., 2009, "Bio-Mimetic Silicone Cilia for Microfluidic Manipulation," Lab Chip, **9**(11), pp. 1561–1566.
[14] Khatavkar, V. V., Anderson, P. D., den Toonder, J. M. J., and Meijer, H. E. H., 2007, "Active Micromixer Based on Artificial Cilia," Phys. Fluids, **19**(8), 083605.
[15] Dreyfus, R., Baudry, J., Roper, M. L., Fermigier, M., Stone, H. A., and Bibette, J., 2005, "Microscopic Artificial Swimmers," Nature (London), **437**(7060), pp. 862–865.
[16] Hill, D. E., and Baumgarten, J. R., 1992, "Control of Spin-Stabilized Spacecraft With Sloshing Fluid Stores," ASME J. Dyn. Syst., Meas., Control, **114**(4), pp. 728–731.
[17] Ibrahim, R. A., 2005, *Liquid Sloshing Dynamics: Theory and Applications*, Cambridge University, New York.
[18] Stokes, G. G., 1850, "On the Effect of the Internal Friction of Fluids on the Motion of Pendulums," Trans. Cambridge Philos. Soc., **9**(2), pp. 8–106.
[19] Ferrers, N. M., ed., 1970, Green's paper on " Researches on the Vibration of Pendulums in Fluid Media," from the Transactions of the Royal Society of Edinburgh, 1833, *Mathematical Papers of George Green*, Chelsea Publishing, New York.
[20] Lindholm, U. S., Kana, D. D., Chu, W.-H., and Abramson, H. N., 1965, "Elastic Vibration Characteristics of Cantilever Plates in Water," J. Ship Res., **9**, pp. 11–22.
[21] Landau, L. D., and Lifshitz, E. M., 1987, "Fluid Mechanics," *Course of Theoretical Physics*, 2nd ed., Pergamon, New York, Sec. 24, Vol. 6.
[22] Stroock, A. D., Dertinger, S. K. W., Ajdari, A., Mezic, I., Stone, H. A., and Whitesides, G. M., 2002, "Chaotic Mixer for Microchannels," Science, **295**(5555), pp. 647–651.
[23] Yaralioglu, G. G., Wygant, I. O., Marentis, T. C., and Khuri-Yakub, B. T., 2004, "Ultrasonic Mixing in Microfluidic Channels Using Integrated Transducers," Anal. Chem., **76**, 3694–3698.
[24] Hawkes, J. J., Barber, R. W., Emerson, D. R., and Coakley, W. T., 2004, "Continuous Cell Washing and Mixing Driven by an Ultrasound Standing Wave Within a Microfluidic Channel," Lab Chip, **4**(5), pp. 446–452.
[25] Grumann, M., Geipe, A., Riegger, L., Zengerle, R., and Ducree, J., 2005, "Batch-Mode Mixing on Centrifugal Microfluidic Platforms," Lab Chip, **5**(5), pp. 560–565.
[26] Herrmann, M., Veres, T., and Tabrizian, M., 2006, "Enzymatically-Generated Fluorescent Detection in Micro-Channels with Internal Magnetic Mixing for the Development of Parallel Microfluidic Elisa," Lab Chip, **6**(4), pp. 555–560.
[27] Vilfan, M., Potočnik, A., Kavčič, B., Osterman, N., Poberaj, I., Vilfan, A., and Babič, D., 2010, "Self-Assembled Artificial Cilia," Proc. Natl. Acad. Sci. U.S.A., **107**(5), pp. 1844–1847.
[28] Sader, J. E., Chon, J. W. M., and Mulvaney, P, 2000,"Experimental Validation of Theoretical Models for the Frequency Response of Atomic Force Microscope Cantilever Beams Immersed in Fluids," J. Appl. Phys., **87**(8), pp. 3978–3988.
[29] Zhang, W., and Turner, K., 2007, "Frequency Dependant Fluid Damping of Micro/Nano Flexural Resonators: Experiment, Model and Analysis," Sens. Actuators, A, **137**, pp. 594–599.
[30] Wang, K.-L., and Jones T.B., 2005, "Electrowetting Dynamics of Microfluidic Actuation," Langmuir, **21**(9), pp. 4211–4217.
[31] Hosseini, M. K. A., Omidi, O., Meghdari, A., and Vossoughi, G., 2006, "A Composite Rigid Body Algorithm for Modeling and Simulation of an Underwater Vehicle Equipped with Manipulator Arms," J. Offshore Mech. Arct. Eng., **128**, pp. 119–132.
[32] Kongthon, J., Mckay, B., Iamratanakul, D., Oh, K., Chung, J.-H., Riley, J. J., and Devasia, S. 2010, "Added-Mass Effect in Modeling of Cilia-Based Devices for Microfluidic Systems," J. Vib. Acoust., **132**, 024501.
[33] Inman D. J., 2001, *Engineering Vibration*, 2nd ed., Prentice-Hall, New Jersey.
[34] Yum, K., Wang, Z., Suryavanshi, A. P., and Yu, M. F., 2004, "Experimental Measurement and Model Analysis of Damping Effect in Nanoscale Mechanical Beam Resonators in Air," J. Appl. Phys., **96**(7), pp. 3933–3938.
[35] Zhang, C., Xu G. , and Jiang, Q., 2003, "Analysis of the Air-Damping Effect on a Micromachined Beam Resonator," Math. Mech. Solids, **8**, pp. 315–325.
[36] Blevins R. D., 1977, *Flow-Induced Vibration*, Van Nostrand Reinhold Company, New York.
[37] Sumer, B. M., and Fredsoe, J., 2006,"Hydrodynamics Around Cylindrical Structures," *Advanced Series on Ocean Engineering*, World Scientific, New Jersey, Vol. 26, revised ed.
[38] Mitra, S., and Sinhamahapatra, K. P., 2007, "Slosh Dynamics of Liquid-Filled Containers With Submerged Components Using Pressure-Based Finite Element Method," J. Sound Vib., **304**(1-2), pp. 361–381.
[39] Nise, N. S, 2004, *Control Systems Engineering*, 4th ed., Wiley, Hoboken, NJ.
[40] Oh, K., Smith, B., Devasia, S., Riley, J. J., and Chung, J.-H., 2010, "Characterization of Mixing Performance for Bio-Mimetic Silicone Cilia," Microfluid. Nanofluid., **9**, pp. 645–655.
[41] Jeon, N. L., Dertinger, S. K. W., Chiu, D. T., Choi, I. S., Stroock, A. D., and Whitesides, G. M., 2000, "Generation of Solution and Surface Gradients Using Microfluidic Systems," Langmuir, **16**, pp. 8311–8316.